# Theoretical Study of Structure and Raman Spectra for Models of Carbon Nanotubes in Their Pristine and Oxidized Forms

**Stephan Irle,[†] Alf Mews,[‡] and Keiji Morokuma*,[†]**

*Cherry L. Emerson Center for Scientific Computation and Department of Chemistry, Emory University, Atlanta, Georgia 30322, and Institut für Physikalische Chemie, Universität Mainz, D-55099 Mainz, Germany*

*Received: July 22, 2002; In Final Form: October 16, 2002*

Changes upon oxidization of carbon nanotubes (CNTs) in structure and Raman spectra are investigated using geometry optimizations and frequency calculations with density functional theory and ONIOM(MO:MO) methods. Macrocycles consisting of six and 12 fused $C_6$ hexagon units, $C_{24}H_{12}$ and $C_{48}H_{24}$ or [6]- and [12]-cyclacene, respectively, were chosen as model systems for zigzag single wall carbon nanotubes. A vertically extended belt model with three fused [12]-cyclacenes, $C_{96}H_{24}$, was also studied as well. The oxidation was modeled by 1,2- or 1,4-cycloaddition poducts of two oxygen atoms at the furthest ends of each macrocycle; 1,4-adducts are found to be much more stable than 1,2-adducts and are possibly the actual oxidation products. It is shown for all these cases that, when oxygen atoms react, the macrocycle undergoes large deformation from the totally symmetric cyclic structure toward an oval shape. This is due to the introduction of $sp^3$ centers on the ring and subsequent relaxation of the adjacent $C_6$ hexagon units. Upon oxidation calculated Raman spectra show large reduction in peak intensities, which can be attributed to the loss of cylindrical symmetry due to structural deformation. The study provides a novel explanation for the experimental observation that Raman spectra of individual CNTs are highly sensitive to oxidization.

## I. Introduction

Since their discovery in 1993,[1,2] single-wall carbon nanotubes (CNTs) have received a large amount of attention as top candidates for molecular "quantum" wires and circuits due to their semiconducting or metallic nature.[3] It is hoped that such beyond-silicon nanotube electronics may lead to unimagined progress in computing miniaturization and power. However, it has proven difficult to control specific structural factors that determine the electronic structure of CNTs, such as diameter and helicity.[4,5] In addition, it was shown[6,7] that exposure to air and oxygen reduces the nanotubes' electrical resistance and increases their thermoelectrical power, but as of yet no detailed structural information is available as to the changes nanotubes undergo upon oxidation. The change of electrical conductivity has been attributed to chemical doping, namely charge-transfer interaction between oxygen molecules and the nanotubes.[6,8,9] However, it remains unclear whether the charge transfer is associated with chemisorbed or physisorbed oxygen.[9] Raman spectroscopy has become a valuable tool to probe structural features of bulk CNTs,[10,11] and it was discovered that Raman scattering of oxidized, metallic nanotubes depends sensitively on the processing conditions.[8] In particular, the position of the two most prominent features of CNT Raman spectra, namely the radial breathing mode near 150 $cm^{-1}$ and the tangential C−C stretch modes around 1580 $cm^{-1}$, which are collectively known as G-band show strong dependence on tube diameter and helicity. For instance, the energy of RBMs has a simple dependence $1/d$, where $d$ is the diameter of the tube.[5] However, until recently the vibrational spectra recorded represented only average properties of nanotube ensembles, and changes in band shapes and intensities are therefore difficult to clearly identify. Two years ago it has become possible to record Raman spectra from individual nanotube bundles or even individual CNTs by using atomic force microscopy in combination with confocal scanning Raman microscopy.[8,12−14] One of the most striking features revealed by applying this technique is that the Raman activity for pristine CNTs was actually decreased by a factor of 4 upon oxidization with $HNO_3$,[13] which might indicate a change in the tube symmetry, thus altering the quantum mechanical selection rules. In addition, FT-IR spectra of ensembles of these compounds show bands between 1650 and 1860 $cm^{-1}$, which have been attributed to C═O bands of lactone functional groups that also could cause a large change in Raman activity.[13] The assignment of these modes to lactone groups is however somewhat arbitrary due to the broad bands of the ensemble's IR spectra. Although investigation of physical properties of CNTs is a rapidly growing field, no further structural information on the chemical nature of the oxidation sites is available yet due to the difficulty in recording well-defined spectra with high resolution and identifying surface effects.

To the best of our knowledge, no serious attempt has been made to simulate Raman spectra of pristine and/or oxidized CNTs at the ab initio level. Simple tight-binding calculations have been able to predict correctly for pristine tubes the high Raman intensities for the RBM near 150 $cm^{-1}$ and the tangential *G*-band modes near 1580 $cm^{-1}$. However, the use of periodicity in these calculations prohibits the investigation of effects of local defects such as five-membered rings or local oxidization sites on the tubes.[15,16] Therefore, we have chosen to perform nonperiodic density functional electronic structure calculations and to carry out geometry optimizations and vibrational frequency and Raman intensity calculations on truncated model systems as representatives of CNTs. We selected macrocycles

[†] Cherry L. Emerson Center for Scientific Computation and Department of Chemistry.
[‡] Institut für Physikalische Chemie.

10.1021/jp026582j CCC: $22.00 
Published on Web 11/12/2002

**SCHEME 1: Valence Bond Structures for the Macrocyclic Ring of Fused $C_6$ Hexagons, [N]-cyclacene, in Their Pristine Form (Top), and 1,2- and 1,4-Oxidized Forms (Bottom)[a]**

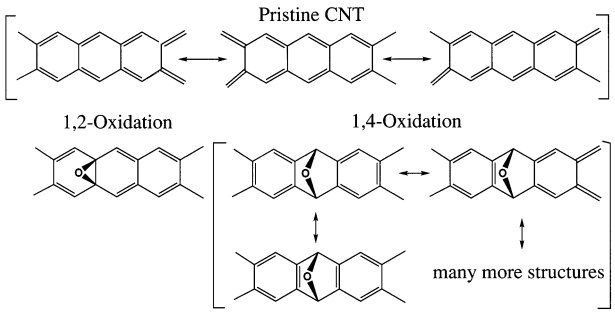


[a] Note the absence of a resonance structure for the 1,2-oxidized species.

of six and twelve fused fully conjugated $C_6$ hexagons, $C_{24}H_{12}$ and $C_{48}H_{24}$, with hydrogens as terminating atoms in the axial ("tube") direction to satisfy the unfilled valences. Such monocyclic systems have been postulated as early as 1985[17] and termed [n]-cyclacenes (n being the number of hexagons)[18] and, therefore, our models are [6]- and [12]-cyclacenes. So far only precursor molecules ([n]-beltenes, [n]-collarenes) without $\pi$-conjugation across the entire macrocycle have been synthesized.[19,20] These structures are commonly regarded as basic cylindrical carbon units of zigzag single wall CNT's.[21] There has been considerable interest in these systems as cyclacenes are proposed to exist in Hückel and Möbius types,[22,23] but in this work we focus only on the structural changes upon oxidation and their effects on Raman spectra. In the case of [12]-cyclacene, we also considered a system, $C_{96}H_{24}$, which is extended in the axial direction by fusing three such cyclacenes, creating a carbon belt with three fused macrocyclic rings consisting of 12 hexagons. For these larger systems we employed the ONIOM[24] (our own N-layer integrated molecular orbital and molecular mechanics) approach for geometry optimizations and second derivative calculations. Using ONIOM, we are able for the first time to calculate ab initio Raman spectra for model systems of nanotubes with local defects that can be extended toward more realistic, larger systems at a reasonable computational cost. In the present case we chose oxidation as local defects due to its large influence on Raman intensities found in experimental Raman spectra of individual CNTs.[13] Due to the unknown chemical nature of the oxidation sites, we settled for modeling the oxidization of these simple systems by 1,2- and 1,4-cycloaddition products, as shown in Scheme 1. We chose these models because they are the smallest possible chemical modification of a nanotube under oxidation with oxygen, and it is also present in lactone groups that are believed to exist in oxidized CNT's. In practice, we used doubly oxidized forms, at two furthest ends of the ring, for the convenience of higher symmetry.

Cyclacenes can be regarded as special cases of fused polyacetylene rings which show no bond length alternations in their pristine form due to the absence of Peierls distortion.[23] Scheme 1 shows two equivalent resonance electronic structures which are responsible for the equivalent bond lengths of carbon−carbon bonds around the macrocycle. From this scheme it becomes obvious that vertical bonds connecting both polyacetylenic macrocycles cannot attain double bond character and hence are much longer. The equal bond lengths of the polyacetylenic subsystems in cyclacenes leads to almost zero singlet/triplet splittings due to the stability of delocalized "solitons" in these systems.[23] Resonance structures of 1,4-type oxidized systems however include structures with partial double bond character in vertical bonds, and a wide variety of them can be formulated (see Scheme 1). Alternations in horizontal bond lengths in the polyacteylenic system should therefore be more pronounced than in the 1,2-type oxidized macrocycles, where even a single fully bonded valence bond structure cannot be drawn that would apply to the entire system and the systems are expected to be less stable.

The calculation of polarizalizability gradient ($\partial^3E/\partial R_i\partial F_\alpha\partial F_\beta$) needed for evaluation of the Raman intensities is computationally expensive especially at the DFT level of theory, because no analytical derivatives of the polarizability ($\partial^2E/\partial F_\alpha\partial F_\beta$) with respect to nuclear coordinates are available. Instead, numerical differentiation of dipole moment derivatives ($\partial^3E/\partial R_i\partial F_\alpha$) with respect to an external electric field has to be performed, giving rise to two additional second derivative calculations of the energy for cylindrically symmetric pristine systems (one radial and one vertical displacement of the field origin) and three additional second derivative calculations of the energy for ellipsoidal structures as in the oxidized species (two radial and one vertical displacements of the field origin). The relatively small models of CNTs represent a compromise between carrying out less accurate calculations on larger, more "tube"-like systems, and highly accurate calculations on even smaller systems. It needs to be stressed that conclusions drawn from the present calculations need to be viewed in the light of being derived from relatively small model systems for CNTs. Extrapolation toward spectra of real CNTs is therefore at present not straightforward. In future calculations, we plan to use semiempirical methods in the low level of ONIOM type calculations, thus making it possible to treat even larger, more tube-like systems. The present study is a pilot for evaluating the use of the ONIOM scheme for such purposes.

## II. Computational Details

Geometry optimizations and frequency calculations were carried out at the B3LYP[25−27] level of hybrid density functional theory, using the standard 6-31G basis set[28] with standard d polarization functions on oxygen atoms. Benchmark geometry optimizations were also performed for the smaller [6]-cyclacene **1_6** using the full 6-31G(d) basis set where polarization functions are included for all atoms. As can be seen from Figure 1, the effect of d functions on carbon is mainly a general tendency to shorter C−C bond lengths by up to 0.005 Å, and the energetic differences are minute with 1.5 kcal/mol. These changes are minute and do not justify the use of d-type polarization functions on carbon atoms. If polarization functions are omitted on oxygen atoms as well, however, C−O bond distances become much longer by up to 0.015 Å and binding energies are weaker by about 5 kcal/mol per oxygen atom. Therefore, we felt comfortable in using the simpler 6-31G basis for carbons and to only include polarization functions for oxygen. We denote this mixed basis set 6-31G(Od). Symmetry restrictions were applied, but no imaginary frequencies were found throughout our calculations. The electronic ground state of most systems studied in this investigation is $S_0$ closed-shell singlet with the exception of the doubly 1,2-oxidized [12]-cyclacene species, which is triplet in its ground state. The singlet−triplet splittings for pristine and doubly 1,2-oxidized forms are small, ranging between −2.5 kcal/mol to 10 kcal/mol. However, to be consistent, we only calculated the Raman spectra for the singlet states in this work. Frequencies were calculated using analytical methods, whereas polarizabilities and

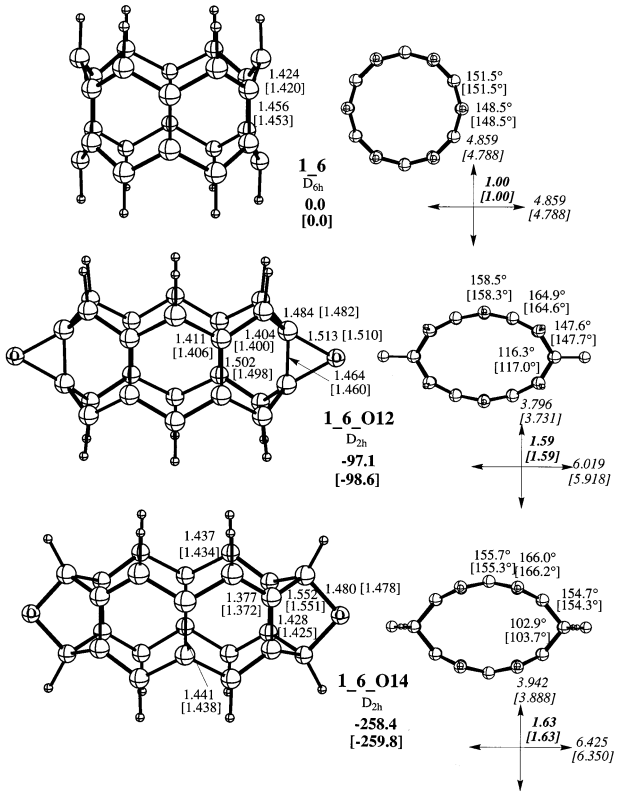


**Figure 1.** Side and top views of the B3LYP/6-31G(Od) optimized geometries of the [6]-cyclacene in the pristine form **1_6** and its doubly oxidized forms **1_6_O12** and **1_6_O14**. Relative energies are given in bold in kcal/mol. On the side view figures, bond lengths are shown in angstroms. On the top view figures, the independent bend angles $\beta$ and the hinge angles $\eta$ are shown alternatively, all in degrees. The bend or hinge angle at the oxidation site is called the kink bend and kink hinge angle. In italics are larger and small diameters (see text for definition) in angstroms, with the ratio of the two in bold italic. Values in square brackets are geometry parameters obtained at the B3LYP/6-31G(d) level of theory.

Raman activities were obtained using a numerical finite field approach. No scaling was attempted, as unmodified B3LYP frequencies are usually per se in good agreement with experimental spectra. The theoretical Raman spectra are presented with overlayed Lorentzian functions with a halfwidth of 2 $cm^{-1}$. For the triple-layered [12]-cyclacene model **3_12** and its oxidized forms, we used the ONIOM (B3LYP/6-31G(Od):B3LYP/STO-3G) method, except that the pure B3LYP/6-31G method was also used for **3_12** for calibration of the ONIOM approximation. Revisions A.7 and A.9[29] of Gaussian 98 were used for the electronic structure calculations and slightly modified to allow for printing Raman intensities larger than $1 \times 10^6$ $Å^4amu^{-1}$.

## III. Optimized Structures

In this section we discuss the B3LYP/6-31G(Od) energetics and optimized structures for pristine and doubly 1,2- and 1,4-oxidized [6]- and [12]cyclacenes as well as the larger triple-layered [12]-cyclacene model and its oxidized forms. To discuss deviation from the perfectly symmetric structures of pristine systems upon oxidation, it is convenient to define the angles in the projection of the carbon skeleton to the plane perpendicular to the principal axis or in the top view of the structures, as illustrated for pristine **1_6** in Figure 1. The hinge angle $\eta$ is the projected angle between two hexagons and the bend angle $\beta$ is the projected angle between the two halves of a single hexagon. For pristine structures with $n$ hexagons arranged in $D_{nh}$ symmetry, the sum $\beta + \eta$ has to be $360 - (360/n)$ degrees. Since the largest changes in the carbon skeleton upon oxidation are fairly localized at the positions where carbon atoms directly bound to oxygens, we will call the associated hinge (for the 1,2-oxidized) and bend angle (for the 1,4-oxidized) the "kink" angle, $\eta_k$ and $\beta_k$, respectively. The oxidized species exhibit a characteristic oval shape with two perpendicular diameters of different lengths across the center of the macrocycles. They have to be defined individually for doubly 1,2- and 1,4-oxidized forms. For doubly 1,2-oxidized species, the larger diameter $D_l$ corresponds to the distance between the two kink hinges with oxygen atoms chemically bound to them on opposite sides of the macrocycle, whereas the shorter diameter $D_s$ is perpendicular to it and is the distance between the center of two hexagons on opposite sides. The situation is reversed in the case of doubly 1,4-oxidized species, where oxygen atoms are located on the center of hexagons on opposite sites with the distance between them being identical to $D_l$, whereas $D_s$ is going through the center of the macrocycle perpendicular to $D_l$. The magnitude of "oval deformation" can then be easily expressed as the ratio between both diameters and is defined here as $R = D_l/D_s$.

The optimized geometries of the [6]-cyclacene and its derivatives are shown in Figure 1. The pristine **1_6** possesses $D_{6h}$ symmetry. Its horizontal C−C bonds on top and bottom of the ring are slightly shorter (∼0.03 Å) than the vertical bonds, which is consistent with the simple valence formula shown in Scheme 1 and the fact that, unlike in graphite, CNTs show two different bond lengths due to the inequivalence of axial and radial directions. Owing to the relative small size of this macrocycle, the ring strain forces the $C_6$ hexagons to adapt the bend angle with $\beta = 148.5°$ and a slightly larger hinge angle with $\eta = 151.5°$, which are 31.5° and 28.5° smaller than a planar conformation with $\beta = \eta = 180.0°$. As can be seen in Figure 1, each hexagon in **1_6** adapts a boat conformation with top and bottom carbon atoms of the boat pointing away from the center of the macrocycle. When two oxygen atoms are added to **1_6** to yield double 1,2- and 1,4-cycloaddition products (**1_6_O12** and **1_6_O14**, respectively), the change in hybridization for the C−O bonded carbon atoms from $sp^2$ to $sp^3$ allows substantial relaxation of the ring strain by introducing a kink into the ring system. **1_6_O14** shows the largest deviation from **1_6** with $\eta_k = 102.9°$, which is decreased by about 46° from $\eta$ of the pristine system. The kink bend angle of **1_6_O12** is larger with $\beta_k = 116.3°$, but still reflects a large change in the chemical environment of the oxidized carbon atoms. Due to these kinks, the unaffected $C_6$ hexagons are allowed to increase both their hinge and bend angles of up to $\eta = 164.9°$ and $\beta = 158.5°$ in **1_6_O12** and up to $\eta = 166.0°$ and $\beta = 155.7°$ in **1_6_O14**. As can be seen in the top views in Figure 1, the overall effect of kink angles and relaxed hinges and bends is that the formerly cyclic rings are deformed to an oval shape when two oxygen atoms are added on opposite sides and form bonds with $sp^3$-hybridized carbon atoms. The degree of oval deformation can be readily expressed by the ratio $R$ defined above, which is 1.00 for **1_6**, 1.59 for **1_6_O12**, and 1.63 for **1_6_O14**, indicating that the 1,4-adduct is slightly more oval and therefore more relaxed than the 1,2-addition product. The stronger structural relaxation in **1_6_O14** is also reflected in its absolute values of the diameters, both of which are larger by 0.406 and 0.146 Å, respectively, than those in **1_6_O12**. Upon looking at the bend and hinge angles in **1_6_O12**, one can see that the hinge angle (147.6°) next to the kink is not much different from that in **1_6**, and the relaxation takes place at the next bend angle and further. The situation is also similar in **1_6_O14**; here the

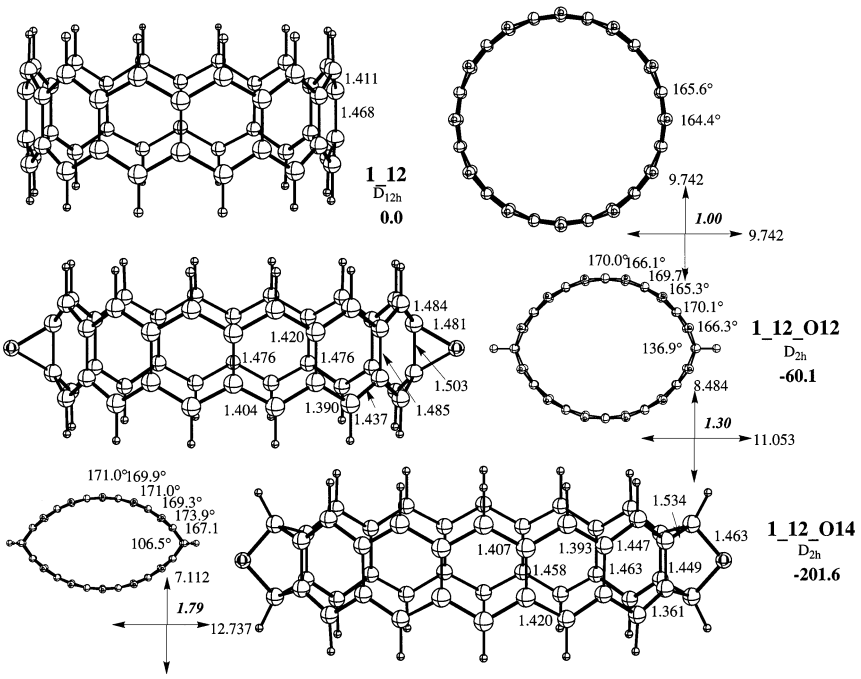


**Figure 2.** Side and top views of the B3LYP/6-31G(Od) optimized geometries of the [12]-cyclacene in the pristine form **1_12** and its doubly oxidized forms **1_12_O12** and **1_12_O14**. See the caption of Figure 1 for details.

bend angle (154.7°) next to the kink is not much different from that in **1_6**, and the relaxation takes place at the hinge angle next to it.

Energetically, the 1,4-adduct **1_6_O14** is predicted to be more than twice as stable as the 1,2-adduct **1_6_O12** with a binding energy of 258.4 kcal/mol with respect to pristine **1_6** and two ($^3$P) oxygen atoms as opposed to 97.1 kcal/mol of the 1,2-adduct. The reason for the large energetic difference is two-fold. First, the three-membered C−O−C ring in **1_6_O12** is highly strained, whereas the two fused five-membered oxygen-containing rings of **1_6_O14** show no indication of ring strain. In fact, the C−O bond in the latter system is much shorter with 1.480 Å than the corresponding bond in the epoxy system with 1.513 Å, indicating a stronger C−O bond. Second, as shown in Scheme 1, the formation of two epoxy groups in the 1,2-cycloaddition reaction with **1_6** completely eliminates the possibility for any resonance structures as opposed to 1,4-cycloaddition. We therefore conclude that **1_6_O14** would be the preferred product of oxidation reactions with oxygen atoms. However, no matter which of both structures is energetically more stable, it is worth noting that for both systems the ring undergoes a clearly visible structural change as a whole when local sp$^3$-hybridized centers or defects are formed by addition reactions, reducing the perfect cylindrical symmetry to a lower one.

The 6-31G(d) results for pristine and oxidized [6]-cyclacenes are remarkably similar to those with the 6-31G(Od), with carbon−carbon bond lengths slightly shorter when d-polarization functions are present. However, the magnitude of the overall change is only about 0.005 Å. Hinge and kink angles are affected only by fractions of a degree, and we therefore felt confident in using the computationally much less expensive 6-31G(Od) basis set.

A six-membered macrocyclic ring with a diameter of only 4.9 Å is certainly too small when comparison is made to real CNTs, where diameters typically range between 11 and 15 Å.[13] The larger model, [12]cyclacene **1_12**, as shown in Figure 2, has a diameter of 9.472 Å, and its properties should therefore be closer to real CNTs. As with **1_6**, this macrocycle displays two different bond lengths, 1.411 Å for the horizontal and 1.468 Å for the vertical C−C bonds. The difference between the two is even larger with 0.057 Å than for **1_6**, where it was only 0.032 Å, indicating an even more pronounced resonance stabilization of the longer polyacetylenic substructure. This finding can be related to the fact that first **1_12** is larger than the six-membered hexagon macrocycles, providing more energetical stabilization of the $\pi$−conjugated system, and second the $C_6$ hexagons are more planar (with $\beta$ and $\eta$ being closer to 180° by about 16° and 14°, respectively) than in **1_6** and hence $\pi$−overlap becomes more pronounced for this larger system. Upon double 1,2- and 1,4-oxidation leading to products, **1_12_O12** and **1_12_O14**, the cyclic rings in the top view become oval as in the case of the six-membered rings, **1_6_O12** and **1_6_O14**. However, **1_12_O12** is less oval with $R = 1.30$ than **1_6_O12** with $R = 1.59$, whereas **1_12_O14** has a more pronounced oval shape with $R = 1.79$ than **1_6_O14** with $R = 1.63$. The reason for the smaller $R$ value of **1_12_O12** is the much wider kink angle with $\beta_k = 136.9°$ as compared to the one of **1_12_O14** with $\eta_k = 106.5°$ and even the one of **1_6_O12** with $\beta_k = 116.3°$. The kink angle in **1_12_O14**, however, is very close to the one found for the six-membered species ($\eta_k = 102.9°$). As was the case for the six-membered ring systems, planarization of $C_6$ units further away from the oxidation site is more pronounced for the 1,4-reaction product. Energetically, the penalty for interruption of the $\pi$−conjugation is more severe due to the more planar $C_6$ hexagons in the pristine system ($\eta = 164.4°$ vs 148.5°), and therefore the binding energies are predicted to be lower with 60.1 and 201.6 kcal/mol for **1_12_O12** and **1_12_O14**, respectively. However, the 1,4-adduct remains still twice more stable than the 1,2-adduct, and would be the preferred product.

To check how much influence adjecent fused rings in the vertical direction have on the magnitude of structural deformation of the oxidized ring, we replaced the hydrogen atoms of **1_12** with macrocyclic $C_{24}H_{12}$ polyacetylene units, to make a three-layer model **3_1**, $C_{96}H_{24}$. We optimized the geometries of pristine **3_12** and doubly 1,2- and 1,4-oxidized **3_12_O12** and **3_12_O14** using the two-layer ONIOM(B3LYP/6-31G(Od):

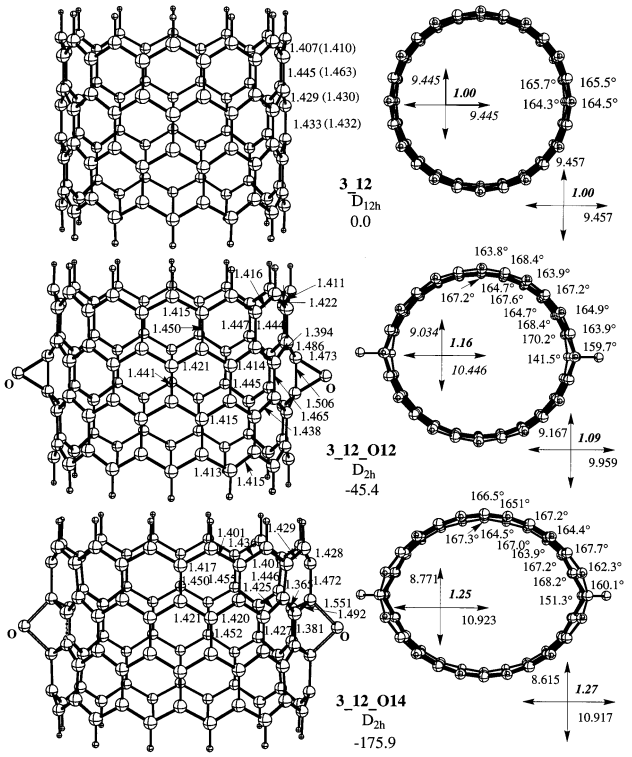


**Figure 3.** Side and top views of the ONIOM(B3LYP/6-31G(Od): B3LYP/STO-3G) optimized geometries of 3-layered belt of [12]-cyclacene **3_12** and its doubly oxidized forms **3_12_O12** and **3_12_O14**. See the caption of Figure 1 for details. For **3_12**, numbers in parentheses correspond to a pure B3LYP/6-31G optimization. For **3_12_O12** and **3_12_O14**, numbers inside the ring correspond to the inner ring, whereas numbers outside correspond to the outer rings.

B3LYP/STO-3G) method, as shown in Figure 3. In the ONIOM scheme, **1_12** was chosen as model system for the high level calculation, whereas the entire system was treated at the less expensive B3LYP/STO-3G level. The reason for keeping the B3LYP method in both layers was to eliminate the need for two different scaling factors for frequencies and intensities.

The pristine structure **3_12** displays much smaller C−C bond length differences for vertical and horizontal bonds in its model system **1_12** with 1.433 and 1.429 Å than the monomacrocyclic system itself with 1.456 and 1.424 Å, respectively. On the other hand, bond length alternation pattern of the outer rings resembles more closely the one of **1_12**, indicating that edge effects are responsible for the large difference of about 0.05 Å in vertical and horizontal C−C bonds. Therefore one would expect that in the nanotube the difference between the horizontal and vertical bond length would be small. A pure B3LYP/6-31G geometry optimization gives qualitatively the same picture, as shown in parentheses in Figure 3, confirming that the ONIOM method is working well for the present system. Upon examining the oxidation products **3_12_O12** and **3_12_O14**, it is found that the oval shape visible in the oxidized monomacrocycles is retained also for these extended system, even though the magnitude of deformation is significantly smaller. The ovalicities for inner and outer macrocycles in **3_12_O12** are $R_i = 1.16$ and $R_o = 1.09$, respectively, while **3_12_O14** shows values of $R_i = 1.25$ and $R_o = 1.27$. The inner kink angle is opened up from 106.5° in **1_12_O14** to 151.3° in **3_12_O14**; this is because the outer layer carbon bound to the oxidized $sp^3$ carbon in **3_12_O14** prevent the latter from twisting outward (as in **1_12_O14**), as seen clearly upon comparison of the top views of the two structures. Interestingly, the hinge angle between the two $C_6$ hexagons immediately above and below the inner kink angle is quite large with $\beta = 160.1°$, yet still following the oval deformation of the inner cycle with a value of $R = 1.27$. In going away from the oxidation site, the outher $C_6$ torsional angles are very similar in magnitude and alternation pattern to the ones of the inner ring. This result suggests that, if localized structural deformation has taken place, the neighboring areas are affected by these changes as well due to the tube's desire to achieve maximum $\pi$-overlapping of the carbon $sp^2$-skeleton. It is therefore relatively easy to achieve large structural deformation of CNTs by introducing localized defects, especially hybridization changes from $sp^2$ to $sp^3$ that occur during chemical oxidation.

**TABLE 1: Principal Values of the Polarizability Tensor for Pristine and Oxidized Species: *x* Corresponds to the Direction of $D_l$, *y* Corresponds to the Direction of $D_s$, and *z* Corresponds to the "Tube" Direction**

| | polarizability tensor elements [bohr$^3$] | | |
|---|---|---|---|
| system | *xx* | *yy* | *zz* |
| **1_6** | 275 | 275 | 279 |
| **1_6_O12** | 359 | 217 | 214 |
| **1_6_O14** | 277 | 140 | 215 |
| **1_12** | 1104 | 1104 | 549 |
| **1_12_O12** | 1353 | 634 | 557 |
| **1_12_O14** | 893 | 374 | 444 |
| **3_12** | 1421 | 1421 | 6181 |
| **3_12_O12** | 1728 | 1296 | 5283 |
| **3_12_O14** | 1233 | 1052 | 4747 |

## IV. Simulated Raman Spectra

In the following paragraph we will qualitatively describe the calculated Raman spectra for the pristine and oxidized model systems and assign characteristic vibrational modes to most important bands. Only the relevant region for carbon related vibrations between 0 and 2000 cm$^{-1}$ will be considered. It should be noted that hydrogen vibrations strongly mix with the motion of the carbon skeleton, and that therefore due to their "artificial presence" in our models these spectra only can provide a qualitative picture of the effects of oxidation. This is especially true for the carbon skeleton motions above 1500 cm$^{-1}$ which are therefore no pure *G*-bands as found in spectra of real CNT's. Due to the very complex nature of these vibrations, it is very difficult to assign a one-to-one correspondence of modes for pristine and oxidized systems. We further will attempt to point out significant differences in Raman spectra between pristine and oxidized form on one hand, and similarities between six-membered and 12-membered macrocycles on the other. In this context we will mainly focus on changes in Raman activities. The relationship of Raman activities and polarizabilities will be briefly discussed using Table 1, which lists the principal elements of the calculated polarizability tensors for all pristine and oxidized species of this study.

Figure 4 shows the calculated Raman spectra of the model systems. These spectra clearly show that the Raman intensities strongly decrease upon oxidation, with the 1,4-oxidized species showing a larger effect than the 1,2-oxidized species. The spectrum of pristine **1_6** exhibits five bands with intensities larger than 200 Å$^4$amu$^{-1}$. Their major features are: vertical carbon−carbon stretching motions at 1527 cm$^{-1}$, horizontal C−C stretches at 1390 cm$^{-1}$, hydrogen bending motions at 1205 cm$^{-1}$, out-of-plane motions of the carbon skeleton around 400 cm$^{-1}$, and hydrogen out-of-plane bends with contributions from carbon at energies lower than 400 cm$^{-1}$. The RBM is located at 146 cm$^{-1}$ and not very Raman active with only 5 Å$^4$amu$^{-1}$

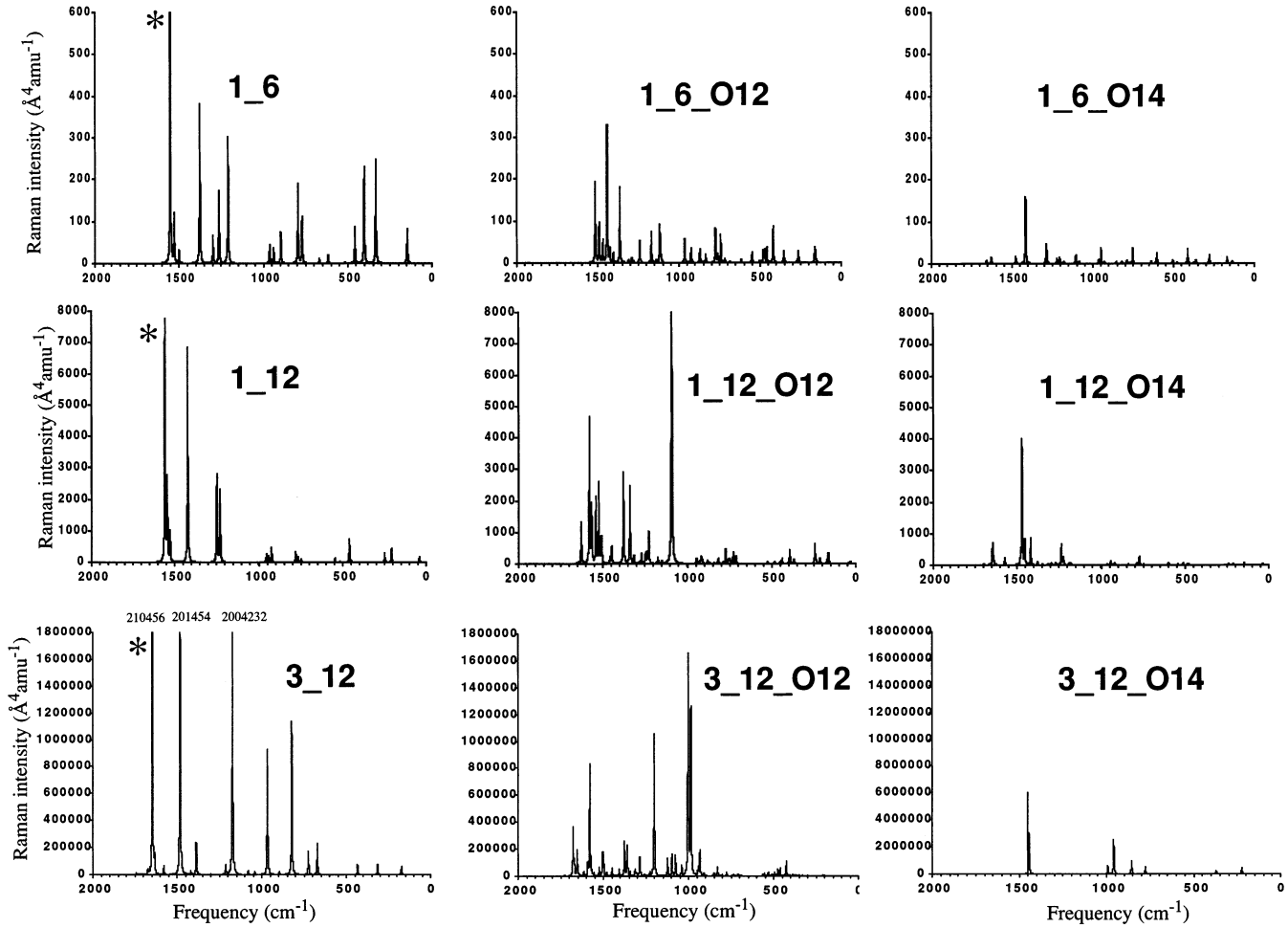


**Figure 4.** Top: Calculated Raman spectra for the [6]-cyclacene **1_6** and its oxidized forms **1_6_O12** and **1_6_O14**. Middle: Calculated Raman spectra for the [12]-cyclacene **1_12** and its oxidized forms **1_12_O12** and **1_12_O14**. Bottom: Calculated Raman spectra for the three-layered belt of [12]-cyclacene **3_12** and its oxidized forms **3_12_O12** and **3_12_O14**. Tangential C−C stretch vibrations corresponding to the experimental G-band are marked by stars.

intensity. The polarizability of **1_6** is almost isotropical with values of 275 and 279 bohr$^3$ for radial and vertical directions, respectively, as the diameter of this macrocycle is similar to its vertical dimension with 4.8 and 5.0 Å, respectively.

The oxidized form **1_6_O12** shows only two bands, which correspond mainly to C−C stretch vibrations of the three-membered oxo-rings at 1509 cm$^{-1}$, and a carbon skeleton stretch vibration around 1440 cm$^{-1}$. Its RBM is unchanged with 158 cm$^{-1}$ in energy and intensity, and the C−O symmetric stretch vibration is located at 944 cm$^{-1}$, exhibiting only very small Raman activity. Especially the Raman activity of the G-band around 1500 cm$^{-1}$ is drastically reduced by about a factor of 2.6, and accompanied by a red shift of about 10−20 wavenumbers. The large reduction in intensity is the most notable difference visible in the difference Raman spectrum. While the principal elements of the polarizability tensor indicate loss of symmetry, their absolute values are of similar magnitude as those calculated for **1_6** with 359 and 217 bohr$^3$ for radial components and 214 bohr$^3$ for the vertical component. The origin of the weaker Raman intensities is therefore clearly related to smaller changes of polarizabilities of Raman active modes and not a consequence of decreased absolute polarizabilities.

Other much less pronounced changes include significant reduction of intensity for the carbon skeleton out-of-plane bands near 400 cm$^{-1}$ and the horizontal C−C stretch frequencies around 1400 cm$^{-1}$. In these cases, the location of the bands does not even change by more than 10 wavenumbers. Among the six-membered macrocycles, **1_6_O14** is the compound that is most deformed by the addition of oxygen atoms, and does not show a single band with an intensity larger than 200 Å$^4$ amu$^{-1}$ in Figure 4. Correspondingly, diagonal elements of the polarizability tensor reflect the large structural deviation from cylindrical symmetry but again are of the same order of magnitude as compared to the pristine system. As for **1_6_O12**, the origin for the much weaker Raman intensities is therefore related to smaller changes of polarizabilities for Raman active modes. This is especially true for the characteristic G-type carbon skeleton stretch vibrations, which are located around 1580 cm$^{-1}$ in this system. The RBM is calculated to be at 167 cm$^{-1}$, even higher than that for **1_6_O12**, indicating an even stronger carbon skeleton due to the larger $\pi$-overlap of the structural distortions introduced by oxidation unaffected six-membered rings. The Raman spectrum only features one very strong peak at 1421 cm$^{-1}$, which is however also reduced in relative intensity by a factor of about 3 when compared to that of **1_6**, similar as that for **1_6_O12**. All other peaks, including the C−C stretch vibrations around 1390 cm$^{-1}$, show very little intensity, and because of their low Raman intensities, the difference spectra for 1,2- and 1,4-oxidized systems (not shown) are almost identical to the spectrum of the pristine system and feature mainly the most prominent peaks of **1_6**.

As can be expected from molecular volume arguments, the larger [12]-cyclacene systems exhibit much higher absolute intensities than the [6]-cyclacene systems. Their spectra are

depicted in the middle part of Figure 4. Especially radial components of the polarizability tensor are larger by a factor of about 3, but the trends in their behavior in going from pristine to oxidized species are very similar compared to the [6]-cyclacene systems. For **1_12** the positions and intensities of the *G*-type peak around 1550 $cm^{-1}$ and the carbon stretch modes around 1390 $cm^{-1}$ are similar in frequencies and relative intensities with their occurrence in the Raman spectrum of **1_6**. This spectrum shows significant similarity with the features of experimental Raman spectra of single-wall CNTs, which are greatly dominated by peaks for RBM and C−C stretch modes around 1300 and 1560 $cm^{-1}$.[10] Especially the C−C out-of-plane bands around 500 $cm^{-1}$ that were very characteristic for the Raman spectrum of pristine **1_6** have lost considerably their Raman intensity. The spectrum of **1_12_O12** is somewhat similar to its analogue **1_6_O12** with a larger energy range for bands around 1500 wavenumbers, but relative intensities for vibrations especially below 1000 $cm^{-1}$ are much smaller and almost negligible. A new feature is a very strong peak at 1091 $cm^{-1}$ with an intensity of 13800 $Å^4$ $amu^{-1}$, which can be assigned to the symmetric C−O stretch mode. The relatively large C−O bond distance of 1.481 Å makes the more flexible carbon skeleton of **1_12_O12** softer at the kink angles as compared to **1_6_O12**, which leads to a greater polarizability for this particular mode. This mode, however, is almost dark in the Raman spectrum of **1_12_O14**, which resembles even more closely the patterns of its six-membered analogue with only one prominent C−C stretch band below 1500 wavenumbers. The intensities of horizontal C−C stretch and C−C out-of-plane modes at lower energies are almost invisible for this species. The effect of reduction of Raman intensity upon oxidation can therefore clearly be observed and is even enhanced in the case of the 12-membered macrocycles. The remainder of the peaks is much less intense, with the RBM extremely weak and red shifted to 48 $cm^{-1}$, which can be attributed to the larger diameter of the macrocycle. The G-band lines are generally blue-shifted by about 20 $cm^{-1}$ relative to the smaller macrocycles. The intensities for the larger system are even smaller from a relative point of view, owing to the greater C−O interaction and a stronger deformation in this case.

As to the Raman spectra of the larger belt systems, shown also in Figure 4, the absolute intensities increase now by 3 orders of magnitude due to their size. Radial components of the polarizability tensors are similar to the monocyclic [12]-cyclacenes, but the polarizability *zz* along the "tube" direction is larger by a factor of about 6. Qualitatively, the spectrum of **3_12** has a similar appearance as its analogue **1_12**, especially for the bands around 1500 and 1300 wavenumbers. However, due to the very large absolute intensity of some of the modes (up to $2 \times 10^6$ $Å^4$ $amu^{-1}$), the bands seem generally to have narrowed even though this is not the case (the energy range for the most dominant peaks is still very similar as compared to [12]cyclacene). Only two vibration bands have gained in intensity due to the extension of the system in axial direction, namely one close to 1000 $cm^{-1}$ and another one around 900 $cm^{-1}$, which are associated with symmetric couplings of C−C stretch vibrations with out-of-plane hydrogen vibrations and should be regarded as an artifact. Given this fact, it is surprising how similar the spectra of pristine [n]cyclacenes and more tube-like species are. However, one should keep in mind that the belt type calculations were carried out using ONIOM with a model system identical to **3_12**.

As found above for the single macrocyclic structures, the Raman intensities of oxidized species are drastically reduced, especially so for the spectrum of **3_12_O14**. Again we find a striking similarity between this spectrum and its analogue for **1_12_O14**, with the only exception that a substantial intensity is associated with a band around 1000 $cm^{-1}$ not present in the monocyclic system. Inspection of the normal modes shows, for example, the case in **3_12**, that hydrogen out-of-plane vibrations are responsible for this large peak. The Raman activities of C−C stretch vibrations responsible for the large peak around 1600 $cm^{-1}$ in **1_12** and **3_12** corresponding to the characteristic G-band in carbon nanotubes are greatly reduced by oxidization, whereas hydrogen-bending modes around 1440 $cm^{-1}$ remain visible as an artifact of the model.

Since the effect of oxidization in our model is most probably overemphasized as compared to experimental conditions, we find a dramatic reduction of Raman activity for C−C stretch vibrations compared to the pristine models. We assume that the experimental spectra (particularly Figure 5 of ref 13) show significant Raman activity for the G-band due to the fact that many areas of the nanotubes are still intact and not affected by oxidization.

## V. Summary and Perspective

We have performed density functional and ONIOM(MO:MO) geometry optimization and frequency calculations on models of single walled carbon nanotubes and their oxidized formed, to gain insight to the changes in geometries and Raman spectra upon oxidation of nanotubes. We have adopted as model systems for nanotubes, macrocycles consisting of six and twelve fused $C_6$ hexagon units, [6]- and [12]-cyclacene, respectively. To take into account the effects of extension to the vertical direction, we also considerd a belt model with three fused [12]-cyclacenes. The oxidation was modeled by double 1,2- or 1,4-cycloaddition poducts. The 1,4-adducts are found to be much more stable than 1,2-adducts and are possibly the actual oxidation products. This finding can be easily explained by the larger number of $\pi$−conjugation valence bond structures for the 1,4-adducts and is reflected in the geometrical parameters. The effects of oxidation on the molecular structures of these model structures for nanotubes is considerable. Upon oxidation, the macrocycle undergoes large deformation from the totally symmetric cyclic structure toward an oval shape. The introduction of $sp^3$ centers on the ring causes a sharp kink in the local structure, and this makes the other part of the ring flatter. This geometrical change is more pronounced in the 1,4-oxidized form than the 1,2-oxidized form. Upon oxidation calculated Raman spectra show large reduction in peak intensities, which can be attributed to the loss of cylindrical symmetry due to structural deformation.

On the bases of these model calculations, we postulate that $sp^3$-type defects introduced by chemical oxidation lead to major changes in the nanostructure. The experimentally observed large decrease in Raman intensities can be explained in terms of structural changes from symmetric tubes to significantly more asymmetric, deformed structures. Our calculated Raman spectra show exatly this tendency, most pronounced for the energetically more stable 1,4-type oxidized species, where this effect is most clearly visible, leading to only one prominent C−C stretch vibration peak in the spectra with almost zero intensity for all other bands. This is visible in difference Raman spectra between pristine and odxidized species, which also clearly indicate similarities between the changes in Raman spectra of 1,2-type and 1,4-type oxidized species.

For now it remains an open question if the distortion of the tube models stems from their short length. Due to the compu-

tational effort for these systems at the ab initio level of theory, it is, however, very costly to include more macrocycles to extend the carbon nanotube. To this end, we are modifying an external ONIOM driver module which will work with the popular MOPAC2002[30] program, and using the patented MOZYME algorithm we will be able to perform geometry optimizations and analytical second derivative calculations on larger, more realistic tubes with the much faster semiempirical AM1 method in the low level layer.

**Acknowledgment.** We thank Prof. Eiji Osawa for very fruitful discussions and literature pointers. This work was partially supported by a grant from the Petroleum Research Fund, the American Chemical Society. Acknowledgment is made to the Cherry L. Emerson Center of Emory University for the use of its resources, which is in part supported by a National Science Foundation grant (CHE-0079627) and an IBM Shared University Research Award. We also thank the National Center for Supercomputing Applications (NCSA) for valuable computer time.

## References and Notes

(1) Iijima, S.; Ichihashi, T. *Nature* **1993**, *363*, 603.

(2) Bethune, D. S.; Kiang, C. H.; deVries, M. S.; Goreman, G.; Savoy, R.; Vazquez, J.; Beyers, R. *Nature* **1993**, *363*, 605.

(3) Dalton, A. B.; Stephan, C.; Coleman, J. N.; McCarthy, B.; Ajayan, P. M.; Lefrant, S.; Bernier, P.; Blau, W.; Byme, H. J. *J. Phys. Chem. B* **2000**, *104*, 10012.

(4) Dresselhaus, M. S.; Dresselhaus, G.; Eklund, P. C. *Science of Fullerenes and Carbon Nanotubes*; Academic Press: New York, 1996.

(5) Saito, R.; Dresselhaus, S.; Dresselhaus, M. S. *Physical Properties of Carbon Nanotubes*; Imperial College Press: London, 1998.

(6) Collins, P. G.; Bradley, K.; Ishigami, M.; Zettl, A. *Science* **2000**, *287*, 1801.

(7) Kong, J.; Franklin, N. R.; Zhou, C.; Chapline, M. G.; Peng, S.; Cho, K.; Dai, H. *Science* **2000**, *287*, 622.

(8) Yu, Z.; Brus, L. E. *J. Phys. Chem. A* **2000**, *104*, 10995.

(9) Jhi, S.-H.; Louie, S. G.; Cohen, M. L. *Phys. Rev. Lett.* **2000**, *85*, 1710.

(10) Rao, A. M.; Richter, E.; Bandow, S.; Chase, B.; Eklund, P. C.; Williams, K. A.; Fang, S.; Subbaswamy, K. R.; Menon, M.; Thess, A.; Smalley, R. E.; Dresselhaus, G.; Dresselhaus, M. S. *Science* **1997**, *275*, 187.

(11) Kasuya, A.; Sugano, M.; Maeda, T.; Saito, Y.; Tohji, K.; Takahashi, H.; Sasaki, Y.; Fukushima, M.; Nishina, Y.; Horie, C. *Phys. Rev. B* **1998**, *57*, 4999.

(12) Mews, A.; Koberling, F.; Basche, T.; Phillip, G.; Duesberg, G. S.; Roth, S.; Burghard, M. *Adv. Mater.* **2000**, *12*, 1210.

(13) Mews, A.; Jiang, C.; Schuessler, T.; Phillipp, G.; Fan, Y.; Burkhard, M. *Isr. J. Chem.* **2001**, *41*, 15−22.

(14) Jorio, A.; Saito, R.; Hafner, J. H.; Lieber, C. M.; Hunter, M.; McClure, T.; Dresselhaus, G.; Dresselhaus, M. S. *Phys. Rev. Lett.* **2001**, *86*, 1118.

(15) Richter, E.; Subbaswamy, K. R. *Phys. Rev. Lett.* **1997**, *79*, 2738−2741.

(16) Saito, R.; Takeya, T.; Kimura, T.; Dresselhaus, G.; Dresselhaus, M. S. *Phys. Rev. B* **1998**, *57*, 4145.

(17) Alder, R. W.; Sessions, R. B. *J. Chem. Soc., Perkin Trans. 2* **1985**, *1985*, 1849−1854.

(18) Godt, A.; Enkelmann, V.; Schlüter, A.-D. *Angew. Chem., Int. Ed. Engl.* **1989**, *28*, 1680−1682.

(19) Ashton, P. R.; Isaacs, N. S.; Kohnke, F. H.; Slawin, A. M. Z.; Spencer, C. M.; Stoddart, J. F.; Williams, D. J. *Angew. Chem., Int. Ed. Engl.* **1988**, *28*, 966−969.

(20) Stoddart, J. F. *Nature* **1998**, *332*, 10.

(21) Kintzel, O.; Luge, P.; Weber, M.; Schluter, A. *J. Org. Chem.* **1998**, *99*, 3001.

(22) Türker, L. *J. Mol. Struct. (THEOCHEM)* **2000**, *531*, 333.

(23) Houk, K. N.; Lee, P. S.; Nendel, M. *J. Org. Chem.* **2001**, *66*, 5517−5521.

(24) Dapprich, S.; Komaromi, I.; Byun, K. S.; Morokuma, K.; Frisch, M. J. *J. Mol. Struct. (THEOCHEM)* **1999**, *461−462*, 1.

(25) Becke, A. D. *J. Chem. Phys.* **1993**, *98*, 5648.

(26) Becke, A. D. *Phys. Rev.* **1988**, *A*, 3098.

(27) Lee, C.; Yang, W.; Parr, R. G. *Phys. Rev.* **1988**, *B 37*, 785.

(28) Hariharan, P. C.; Pople, J. A. *Theor. Chim. Acta* **1973**, *28*, 213.

(29) Frisch, M. J.; Trucks, G. W.; Schlegel, H. B.; Scuseria, G. E.; Robb, M. A.; Cheeseman, J. R.; Zakrzewski, V. G.; Montgomery, J. A., Jr.; Stratmann, R. E.; Burant, J. C.; Dapprich, S.; Millam, J. M.; Daniels, A. D.; Kudin, K. N.; Strain, M. C.; Farkas, O.; Tomasi, J.; Barone, V.; Cossi, M.; Cammi, R.; Mennucci, B.; Pomelli, C.; Adamo, C.; Clifford, S.; Ochterski, J.; Petersson, G. A.; Ayala, P. Y.; Cui, Q.; Morokuma, K.; Malick, D. K.; Rabuck, A. D.; Raghavachari, K.; Foresman, J. B.; Cioslowski, J.; Ortiz, J. V.; Stefanov, B. B.; Liu, G.; Liashenko, A.; Piskorz, P.; Komaromi, I.; Gomperts, R.; Martin, R. L.; Fox, D. J.; Keith, T.; Al-Laham, M. A.; Peng, C. Y.; Nanayakkara, A.; Gonzalez, C.; Challacombe, M.; Gill, P. M. W.; Johnson, B. G.; Chen, W.; Wong, M. W.; Andres, J. L.; Head-Gordon, M.; Replogle, E. S.; Pople, J. A. *Gaussian 98*; Gaussian, Inc.: Pittsburgh, PA, 1998.

(30) Stewart, J. J. P. *MOPAC2002*; Fujitsu Limited: Tokyo, Japan, 1999, 2001.